Force and velocity fluctuations over rough foils at moderate Reynolds numbers

Kurt, Melike; Vilumbrales-García, Rodrigo; Weymouth, Gabriel; Ganapathisubramani, Bharathram

DOI
10.1007/s00348-025-04124-8

Publication date
2025

Document Version
Final published version

Published in
Experiments in Fluids

Experiments in Fluids (2025) 66:198
https://doi.org/10.1007/s00348-025-04124-8

RESEARCH ARTICLE

Force and velocity fluctuations over rough foils at moderate Reynolds numbers

Melike Kurt[1] · Rodrigo Vilumbrales-García[1,2] · Gabriel Weymouth[3] · Bharathram Ganapathisubramani[1]

Received: 2 August 2024 / Revised: 18 September 2025 / Accepted: 20 September 2025

Abstract

Surface roughness modifies the flow dynamics over static surfaces and can significantly affect the instantaneous generation of lift and drag. This study presents force and flow measurements on NACA0012 foils covered with simple, commercially available spherical-cap roughness elements. We varied the roughness area coverage relative to the propulsive area from 0% (smooth) to 35% (mid-rough) and 70% (full-rough). Our experiments survey an angle of attack and a Reynolds number range of $-2° \leq \alpha \leq 20°$ and $10{,}000 \lessapprox Re \lessapprox 55{,}000$, respectively. Within this parameter space, surface roughness leads to small alterations in time-averaged statistics of lift and drag. In contrast, it leads substantial changes in unsteady force and flow behavior. Specifically, surface roughness reduces lift fluctuations, up to $\sim 60\%$, due to decreased pressure fluctuations on the foil surface. This reduction is accompanied by a modest decrease in time-averaged lift coefficient and an increase in time-averaged drag coefficient. Drag fluctuations increase by up to $\sim 30\%$, except near stall, where both lift and drag fluctuations decrease. Roughness also mitigates flow separation, as indicated by reduced velocity fluctuations and a delayed stall onset in the $C_L(\alpha)$ curves. These results show that surface roughness influences not only time-averaged statistics but also the instantaneous response of lift, drag, and flow fields. Our findings offer insights into the hydrodynamic function of shark-skin-inspired surfaces and demonstrate how simple, distributed roughness can provide passive control of boundary layer behavior and flow separation.

1 Introduction

Surface roughness is ubiquitous in nature and, inevitably, in engineering applications. Consideration of surface roughness and investigation of its influence on flow dynamics and drag production are crucial for wide-ranging applications. From pipe flows (Colebrook and White 1937; Moody 1944) and cross-flow around cylinders (Achenbach 1971) to dimples on golf balls (Bearman and Harvey 1976; Chowdhury et al. 2016), a football (Ward et al. 2023) or swimsuit designs (Moria et al. 2010), the influence of surface roughness has been the subject of research interests across the board. The presence of surface roughness can have detrimental effects on the performance of engineering systems. Bio-fouling around ship hulls causes a gradual increase in drag over time and poor fuel performance (Monty et al. 2016; Hutchins et al. 2023). The accumulation of sediments around wind turbine (Ehrmann et al. 2017) or tidal turbine blades (Walker et al. 2014) leads to a reduction in power extraction and a performance decrease that is linked to an increase in roughness density and height. Icing on airfoils, particularly around the leading edge region, causes early flow separation and poor lift performance (Vinnes and Hearst 2021), threatening the life cycle of wind turbine blades and airplane wings. Given these warning signs, it is not surprising that a growing body of literature seeks to understand the role of surface roughness through numerous investigations of its function on biological systems (Bechert et al. 2000), its interaction

✉ Melike Kurt
m.kurt@soton.ac.uk

Rodrigo Vilumbrales-García
rodrigga@umich.edu

Gabriel Weymouth
g.d.weymouth@tudelft.nl

Bharathram Ganapathisubramani
g.bharath@soton.ac.uk

[1] Faculty of Engineering and Physical Sciences, University of Southampton, University Road, Southampton SO17 1BJ, UK

[2] Naval Architecture and Marine Engineering, University of Michigan, Ann Arbour, MI 10587, USA

[3] Faculty of Mechanical, Maritime and Materials Engineering (3mE), TU Delft, 2628 CD Delft, The Netherlands

Published online: 09 October 2025

with turbulent boundary layer flows (García-Mayoral and Jiménez 2011; Chung et al. 2021), and its potential applications on aerodynamic control surfaces (Gad-el Hak and Bushnell 1991) to inform the design of passive and active flow control devices.

From feathered flight (Van Bokhorst et al. 2015) and scales on fish (Muthuramalingam et al. 2020) to denticles on sharks (Afroz et al. 2016; Domel et al. 2018a, b; Santos et al. 2021), or tubercles on whales (Miklosovic et al. 2004), the biological world demonstrates an endless combination of scales, shapes and forms. These bioinspired surfaces have been reported to benefit from surface roughness in the form of drag reduction (Domel et al. 2018b), increase in lift-to-drag ratio (Domel et al. 2018a), delay in static or dynamic stall (Van Bokhorst et al. 2015; Miklosovic et al. 2004; Hrynuk and Bohl 2020), delay in transition to turbulence (Muthuramalingam et al. 2020) and flow separation control (Van Bokhorst et al. 2015; Afroz et al. 2016; Santos et al. 2021).

Numerous studies have investigated the effects of complex surface textures on turbulent boundary layers, with particular attention to their potential for reducing skin friction and drag (Chung et al. 2021). It has been shown that surface textures such as longitudinal riblets, once properly scaled (García-Mayoral and Jiménez 2011), can lead to reduced wall shear stresses and skin friction (Choi et al. 1993; Bechert et al. 2000; Dean and Bhushan 2010; García-Mayoral and Jiménez 2011), by restricting the spanwise motion of near-wall structures, reducing turbulent momentum transfer near the wall and creating a viscous sublayer buffer that turbulent eddies cannot penetrate as easily.

Since their introduction in the 1940 s (Taylor et al. 1947), vortex generators (VGs) have been widely employed in classical aerodynamics to mitigate local flow

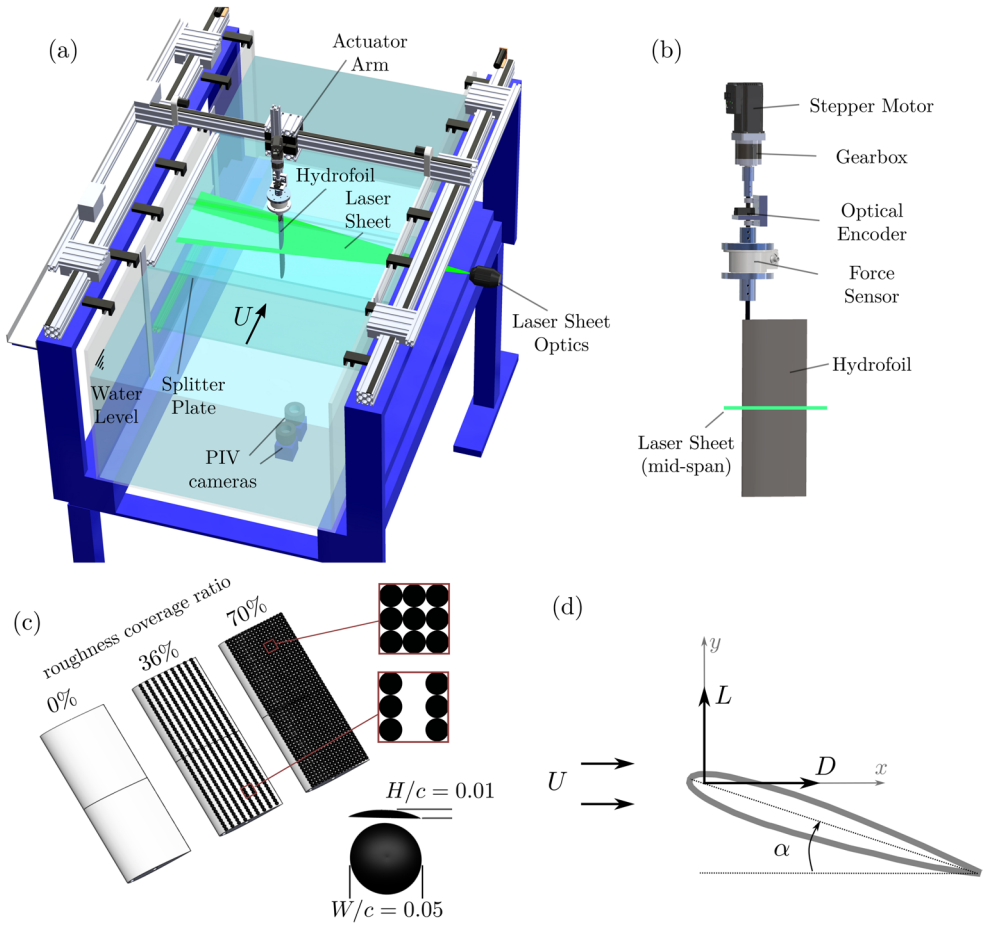

Fig. 1 **a** A schematic of the experimental setup and test section showing the orientation of the PIV measurement plane relative to the hydrofoil. Note that the laser sheet does not illuminate the region behind the hydrofoil where no flow information could be captured. **b** A schematic of the actuation mechanism, manipulating the angle of attack of the hydrofoils. The laser sheet illuminated the hydrofoil cross-section at its mid-span, as indicated by the green line. **c** Schematics of the hydrofoils with different surface coverage for smooth foil (0%), mid-rough (36%) and full rough (70%) with a schematic showing the geometry of the individual spherical cap bumpers used on the foil surfaces. Note that spherical-cap roughness elements are aligned in their rows for both rough foil cases. **d** A schematic presenting the direction of the lift and drag forces measured relative to the hydrofoil and the direction of the free-stream velocity

Table 1 A comparison of the protrusion height and streamwise width of the roughness elements in the relevant literature and the present work for a given chord-based (or length-based) Reynolds number range of interest

	Domel et al. (2018a)	Du et al. (2022)	Lin (2002)	Present work
W/*H*	~ 0.34	~ 0.39	4, 5, ..., 12	5
H[mm]	~ 0.67, ~ 1.35, ~ 2.03	0.94	–	1.6
Re	40,000	20,000	20,000, ..., 500,000	13,000,..., 53,000

separation on lifting surfaces. Typically arranged as rows of small plates or airfoil-shaped elements angled to the flow, their effectiveness depends on their height relative to the boundary layer thickness, (h/δ). High-profile VGs ($h/\delta \sim 1$) offer strong local control but increase profile drag. To address this, Kuethe (1972) demonstrated that low-profile VGs ($h/\delta = 0.27$ and 0.42) can exert a longer range influence, reducing wake deficits by suppressing von Kármán vortex formation. Subsequent studies confirmed that low-profile VGs ($0.1 \leq /\delta \leq 0.625$) balance effective separation control with reduced drag penalties (Lin 2002). Departing from these conventional devices, recent work has explored distributed roughness as a flow control strategy, often inspired by biological surfaces. Examples include shark skin samples (Afroz et al. 2016; Santos et al. 2021; Guo et al. 2021) and 3D-printed biomimetic textures (Domel et al. 2018a, b; Du et al. 2022). Afroz et al. (2016) showed that shark skin reduces separation regions, while (Lang et al. 2008) demonstrated that vortex formation between bristled denticles enhances near-wall momentum and reduces shear stress. On flat plates, Du et al. (2022) found that biomimetic scales with fixed tilt angles delay stall and mitigate adverse pressure gradients. Similarly, Domel et al. (2018b) reported that properly scaled shark-inspired textures can reduce drag on NACA airfoils at low to moderate Reynolds numbers, whereas oversized textures increase drag. Their follow-up study (Domel et al. 2018a) showed that suction-side placement of such scales can improve lift-to-drag ratios, performing comparably to micro VGs (Gad-el Hak and Bushnell 1991; Lin 2002).

Despite these advances, most studies emphasize time-averaged flow and force statistics, overlooking the instantaneous dynamics that are crucial for unsteady maneuvering and flow control. Understanding how roughness elements affect the transient lift and drag response, as well as the corresponding velocity and pressure fields, remains a relatively unexplored area, particularly for aerodynamic or hydrodynamic control surfaces operating at moderate Reynolds number conditions. Additionally, biomimetic textures often introduce challenges in fabrication, parameterization, and directional sensitivity. The high-resolution 3D printing required to replicate biological features such as scale bristling or riblet alignment presents significant manufacturing hurdles (Yasuda et al. 2019). Many of these surfaces are inherently directional, making them less suitable for applications involving variable flow orientation or multi-degree-of-freedom motion. Recent efforts to address these limitations have investigated surface-symmetric roughness elements under dynamic conditions, such as pitching hydrofoils (Vilumbrales-Garcia et al. 2024) or undulatory motion (Massey et al. 2023), using idealized egg-carton-like textures or parametric geometries.

In this study, we aim to isolate and understand the influence of surface roughness coverage and distribution on static hydrofoils using commercially available spherical-cap roughness elements. These elements are geometrically simple, surface-symmetric, and lack directional bias, enabling us to avoid the secondary complexities introduced by biomimetic textures. Our approach focuses on both time-averaged and instantaneous lift, drag forces and flow fields to provide a more comprehensive picture of how roughness affects flow dynamics over a finite foil surface with a well-known NACA cross-section. In the following, we introduce the experimental methodology and the considered parameter space in Sect. 2. In Sect. 3, first, we compare the time-averaged lift and drag measured from

Table 2 Summary of the experimental parameters used in the current study

Parameters						
U [m/s]	0.095	0.123	0.156	0.195	0.234	0.376
Re	13,000	17,000	22,000	27,500	33,000	53,000
α	−4° to 20°		2° increments			
c [m]	0.16					
AR	2.5					

For brevity, we have provided the range of interest for α

hydrofoils with different surface roughness distributions. This is followed by an analysis of force fluctuations. Second, we present a flow analysis considering time-averaged velocity fields and reconstructed pressure fields, comparing the foil surfaces. Section 4 discusses the results from force and flow measurements and establishes connections to fluctuating velocity and pressure fields, followed by Sect. 5 with concluding remarks.

2 Experiment design and methodology

Force and flow measurements were conducted in a recirculating, open surface water channel facility with a cross-section of 1.2 m width and 0.8 m depth, located at the University of Southampton, Boldrewood Innovation Campus. Three identical foils with a rectangular planform and a NACA0012 cross-section were 3d-printed using PolyLactic Acid (PLA) filaments with an infill density of 70% and designed with a chord length of $c = 0.16$ m and aspect ratio of $AR = 2.5$. The suction and pressure sides of the foils were covered with spherical cap roughness elements with a protrusion height of $H = 0.01c$ and a diameter of $W = 0.05c$. The size of the roughness elements was selected to align with previously published studies (please see Table 1) and ensure commercial availability.

Foil surfaces were placed against the bottom wall of the channel with a splitter plate installed on the water surface to constrain the flow around foil tips and enforce nominally two-dimensional flow, as shown in Fig. 1a. Two different roughness cases were considered where the roughness area coverage relative to the total planform area is varied from 36% to 70%. As shown in Fig. 1c, the ratio of 75% corresponds to the case where the entire planform area is covered with adjacent rows of roughness elements in chordwise and spanwise directions. 36% coverage is obtained simply by removing alternating rows of roughness elements in chordwise direction. The rest of the text will refer to these foils with 36% and 70% surface roughness as mid-rough and full-rough, respectively. Additionally, a foil with a smooth surface, with effectively 0% roughness coverage, was considered to establish a baseline. Since the roughness elements are placed on the smooth foil surface, the measurements obtained for the smooth foil surface is considered as the reference and used in comparison to the data obtained for the mid-rough and full-rough foils. Free-stream velocity, U, was varied between six different values corresponding to chord-based Reynolds number values within $13{,}000 \leq Re \leq 53{,}000$, as tabulated in Table 2. The Reynolds number is defined as $Re = Uc/\nu$, where ν is the kinematic viscosity and is calculated for bulk water temperature of 15°C. The measurements were taken at each Re, as the foils' angle of attack was varied within the range of $-4° \leq \alpha \leq 20°$ with 2° increments. The α range is limited to observe pre-stall and stall conditions for the smooth and rough foils within the Re range of interest. The negative α values are included in the parameter space to ensure and check for *zero-lift generation at* $\alpha = 0°$ for this symmetric NACA cross-section in the measurements. The angle of attack cases for $\alpha > 20°$, where the foil surface is well into post-stall conditions, is considered out of the scope of this work.

2.1 Force measurements

We used two six-axis force sensors with different measurement ranges to ensure sufficient resolution and prevent strain-gauge saturation. ATI Mini40 was preferred for the lower Re range, at $Re = 13{,}000$ and 17,000, whereas ATI Gamma was used for higher Re, $22{,}000 \leq Re \leq 53{,}000$. Lift and drag forces are sampled at 1000 Hz. The tests were conducted for the duration of at least 100 convection cycles ($T = c/U$) and repeated 5 times to ensure convergence in the second-order statistics (fluctuations). To confirm that the individual tests are sufficiently long and representative of the problem, we compared the average fluctuations and power spectra calculated from *shorter* tests with an additional set of *longer* trials for two angles of attack, $\alpha = 8°$ and $\alpha = 12°$, obtained over ~ 500 convection cycles at $Re = 13{,}000$. A comparison of PSD curves is given in Fig. 13. At this Re, the RMS values from short trials are within 10 to 20% of the RMS values obtained from the longer tests.

The acquired force data are filtered using a simple FFT (Fast Fourier Transform) scheme with a cut-off frequency defined as $f = kU/(c\sin(\alpha))$ and adjusted to match the same reduced frequency, $k = 0.5$, at each Re to ensure dynamic similarity, except for $\alpha = 0°$ cases where the data is filtered at $f = 4$ Hz. The filtered data sets are then bootstrapped to generate five randomly distributed samples with the same length as the initial data sets. This additional step was necessary to ensure random data distribution to determine average fluctuations for the force coefficients, especially at higher angles of attack, where intermittent flow events such as laminar separation bubble formation or bursting may be present in individual tests. The mean force coefficients were then calculated as the average of 5 time-averaged values obtained from 5 bootstrapped samples. The definition of the drag and lift coefficients are given as follows:

$$C_D = \frac{\overline{D}}{\frac{1}{2}\rho U^2 c^2 AR}, \qquad C_L = \frac{\overline{L}}{\frac{1}{2}\rho U^2 c^2 AR}, \tag{1}$$

where $\overline{(.)}$ denotes the time-averaged values of drag and thrust forces from each test.

The root mean square (RMS) values of fluctuations in lift and drag forces were obtained from the 5 bootstrapped samples for each angle of attack and surface roughness combination.

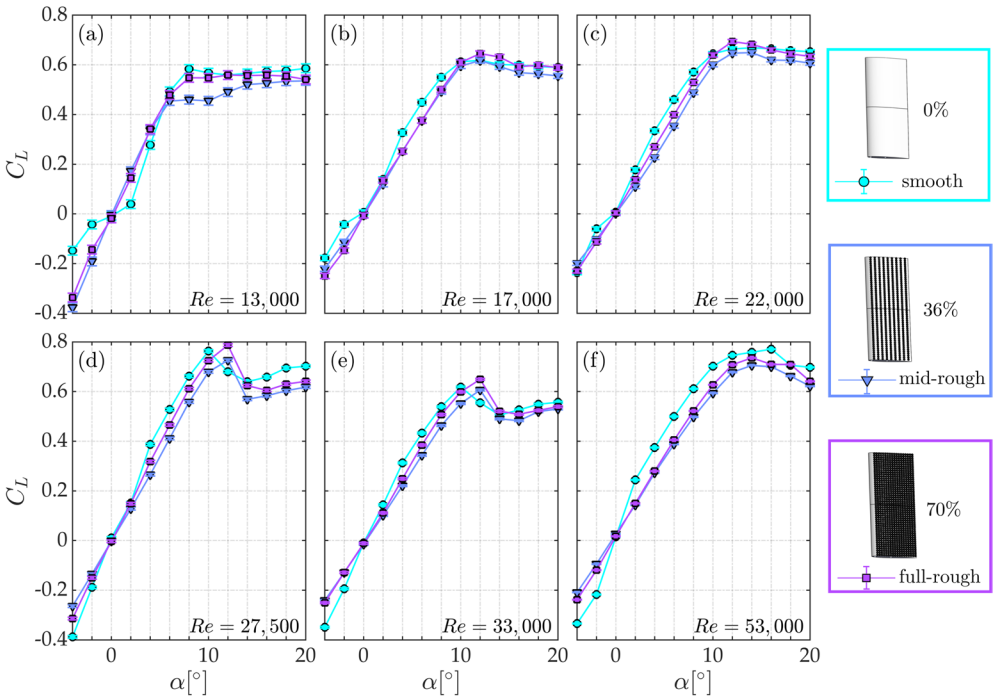

Fig. 2 Mean lift, C_L, as a function of angle of attack, α, at six different Re within the range of $13{,}000 \leq Re \leq 53{,}000$ in ascending order from a to f. Three foils with different surface roughness ratios, smooth (0%), mid-rough (36%) and full-rough (70%), are plotted with three different symbols, •, ▼, and ■, respectively, as mapped to three different colors shown on the right side of the figure. The errorbars are calculated based on t-distributed error with 95% confidence from 5 repeated tests, as $2.776\sigma_{(.)}/\sqrt{5}$. Here, $\sigma_{(.)}$ is the variation from the reported C_L data point or RMS of 5 time-averaged C_L values

As a metric for the fluctuating component of the drag and lift forces, we report the average of RMS values at each α and Re in a non-dimensional form, as $C_D{}'$ and $C_L{}'$, respectively.

2.2 Flow measurements: particle image velocimetry(PIV)

Flow measurements were conducted using a planar PIV system. Two 4-megapixel *LaVision MX* cameras with 50 mm *Nikon* lenses ($f = 5.6$) were placed underneath the water channel as shown in Fig. 1a. The two cameras were arranged side-by-side in the streamwise direction and calibrated at full resolution (2048×2048 pixels), capturing image pairs with a field-of-view of about $2c \times 1c$ with $0.2c \times 1c$ overlap between the camera frames and a digital resolution of 0.087 mm/pixel. The captured area consists of the entire foil cross-section and an additional $0.5c$ in the foils' upstream and downstream regions. A laser beam output by a *Litron Nano PIV* laser head with 200 mJ power output at 532 nm wavelength illuminated the field of view through a set of sheet-forming optics at the foils' mid-span as shown in Fig. 1a.

A pulse timing unit was used to synchronize the laser and the camera triggers and controlled via *DaVis 10* software to record the image pairs. The flow was seeded with polyamide particles with a nominal diameter of 55 μm. The seeding density was iteratively adjusted to have a satisfactory number of particles in the field of view. The image pairs were captured at a frequency of 15 Hz. In total, 1440 and 720 image pairs were collected at $Re = 27{,}500$ and 53,000, corresponding to ~ 117 and ~ 113 convection cycles, respectively. The acquired particle image pairs were filtered using a temporal Butterworth high-pass filtering with a cut-off frequency of 10 Hz, mainly to eliminate surface reflections. The images were then cross-correlated using *DaVis 10* with the final interrogation window size of 24×24 pixels and 50% overlap. The cross-correlation produced velocity fields with 171×171 vectors with a vector spacing $\Delta x = \Delta y = 1.05$ mm. The final velocity fields from each camera were stitched and blended using half a Hanning window over the overlapped region. Based on subpixel accuracy of 0.05 pixels, the biased uncertainty of the PIV fields can be determined as approximately 4.4 mm/s, corresponding to 1.1% of the free-stream velocity at chord-based Reynolds number, $Re = 53{,}000$. Based on smooth foil boundary layer thickness at the trailing edge ($x/c = 1$) at $Re = 53{,}000$, the boundary layer was resolved with 346 pixels with digital resolution of 11.4 pixel/mm.

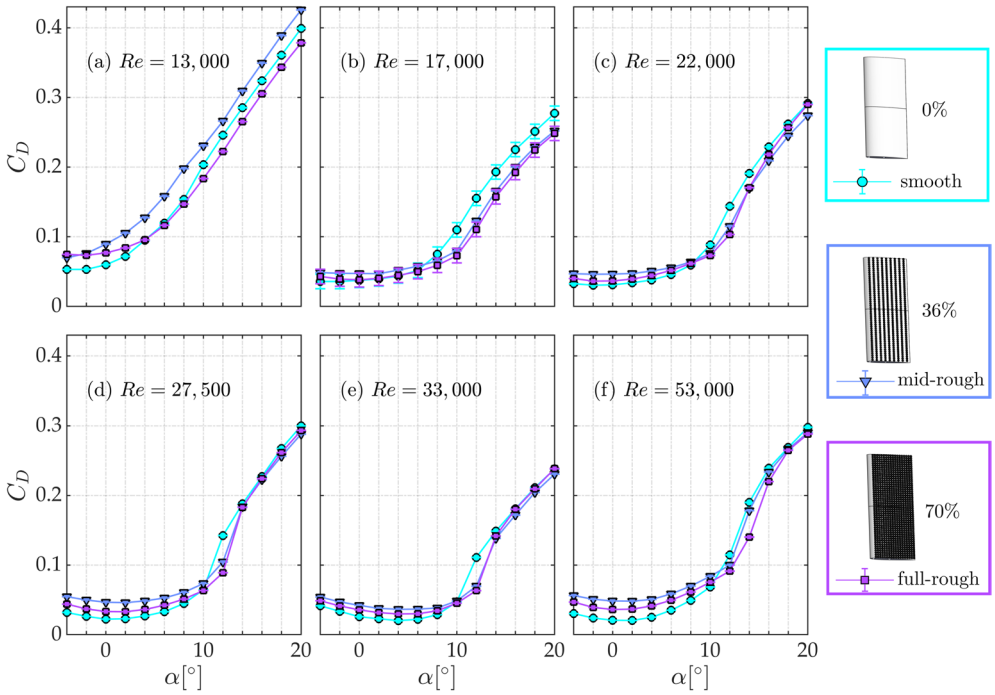

Fig. 3 Mean drag, C_D, as a function of angle of attack, α, at six different Re within the range of $13{,}000 \leq Re \leq 53{,}000$ in ascending order from a to f. Three foils with different surface roughness ratio; smooth (0%), mid-rough (36%) and full-rough (70%), are plotted with three different symbols, •, ▼, and ■, respectively, as mapped to three different colors shown on the right side of the figure. The errorbars are calculated based on t-distributed error with 95% confidence from 5 repeated tests, as $2.776\sigma_{(.)}/\sqrt{5}$. Here, $\sigma_{(.)}$ is the variation from the reported C_D data point or RMS of 5 time-averaged C_D values

3 Results

3.1 Time-averaged lift and drag coefficients

In this section, we present mean and fluctuating components of lift and drag coefficients measured for smooth, mid-rough and full-rough foils for a range of angles of attack and Reynolds numbers, $-4 \leq \alpha \leq 20°$ and $13{,}000 \leq Re \leq 53{,}000$, respectively, as detailed in Table 2. Figure 2a to f shows time-averaged lift coefficients as a function of α at six different Re. Smooth, mid-rough and full-rough foil data are plotted as mapped to different colors.

Traditionally, the lift coefficient is expected to increase linearly with the angle of attack until it reaches the stall point, after which an abrupt drop in lift coefficient occurs, particularly for the high Re range as widely documented (Knight and Wenzinger 1929). Within low to moderate Re range, deviations from this conventional behavior can occur (Lissaman 1983; McMasters and Henderson 1979; Hrynuk et al. 2024). Beyond the stall point, instead of an immediate decline, the lift coefficient may plateau (cease to increase) or increase at a lower slope angle after a brief decline (Menon and Mittal 2020; Hrynuk et al. 2024). Additionally, C_L can increase nonlinearly against α at low angles of attack (Hrynuk et al. 2024). Our dataset reflects these deviations, particularly with the smooth foil exhibiting a non-linear behavior for $\alpha \leq 6°$ across the Re range considered. In the lower Re range, $13{,}000 \leq Re \leq 22{,}000$, the lift plateaus after reaching a peak value for all the foil surfaces. Within this Re range, the $C_L(\alpha)$ lines show small alterations between the foil surfaces, except for the mid-rough foil, which experiences an earlier plateau compared to the smooth and full-rough cases at $Re = 13{,}000$. At higher Re values (27,500 and 33,000) and $\alpha > 14°$, lift increase resumes on a lower slope after a drop in lift coefficient at about $\alpha = 12°$. As Re increases, the maximum lift generated by the foil surfaces gradually rises from approximately $C_{L,\max} \approx 0.6$ at $Re = 13{,}000$ to around $C_{L,\max} \approx 0.8$ at $Re = 53{,}000$.

Beyond the Re dependent modifications, small alterations exist between different surface roughness cases. Smooth foil generates 5 to 30% for $\alpha > 4°$, compared to rough foils across the Re range considered. This difference in lift generation becomes more prominent as Re increases. All three foils show similar trends of $C_L - \alpha$ with some subtle differences. At $Re = 13{,}000$, mid-rough generates up to $\sim 25\%$ lower lift than the other foil surfaces for $\alpha > 6°$. At $Re = 27{,}500$ and 33,000, there is a clear delay in stall for mid-rough and full-rough compared to smooth foil.

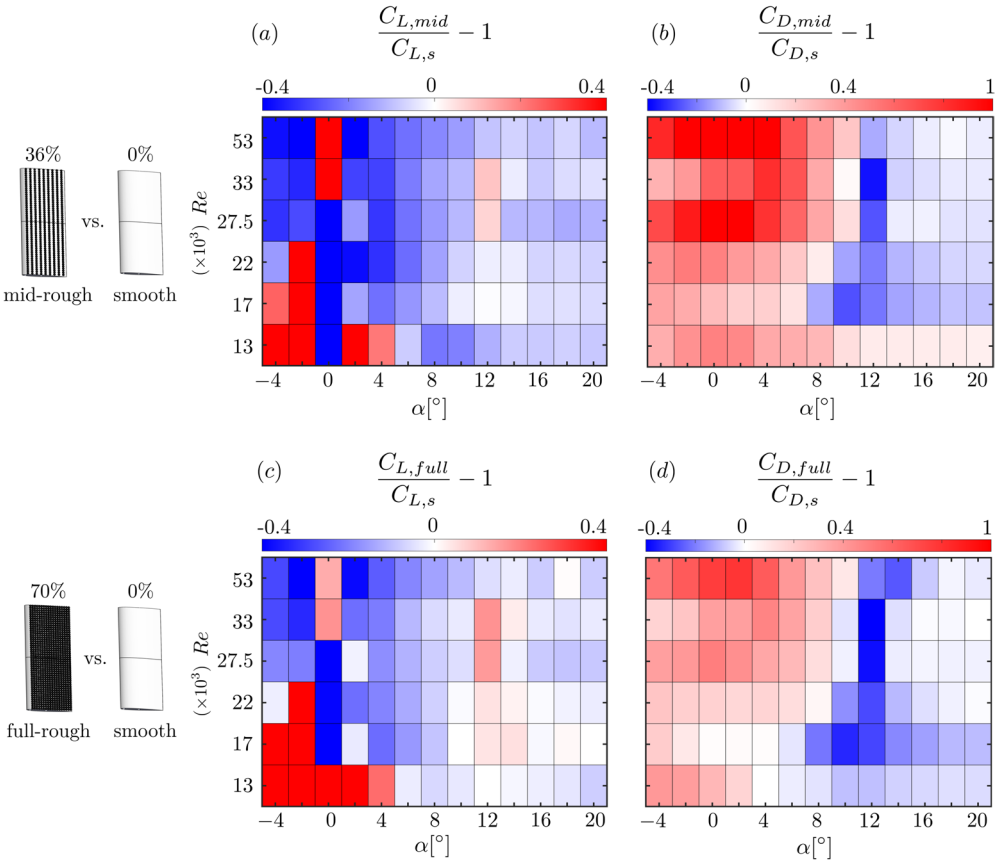

Fig. 4 Time-averaged lift and drag coefficients (first and second columns, respectively) of mid-rough (**a**, **b**) and full-rough (**c**, **d**) foils relative to the smooth foil plotted as heat-maps as functions of α and Re. Each tile color in the heat maps corresponds to a value for a given α and Re

Figure 3 shows the evolution of drag coefficient as a function of α for three different roughness cases across the Re range considered. Overall, the drag coefficient decreases as Re gradually increases from 13,000 to 53,000 in pre-stall conditions. As expected, C_D increases rapidly after the stall-point, up to $C_D \approx 0.4$ at $Re = 13{,}000$ and $C_D \approx 0.24$ at $Re = 33{,}0000$. The drag buckets framed by $C_D - \alpha$ curves become larger as Re increases, as the post-stall increase in C_D becomes non-linear. The drag coefficient for all foil surfaces reaches the highest values at $\alpha = 20°$, the highest angle of attack considered, at any given Re. The highest C_D measured stays within the range of $0.2 \leq C_D \leq 0.3$ for all Re considered, except for $Re = 13{,}000$ at which the measured C_D is much higher than the rest of the parameter space, with $C_D \sim 0.41$ for mid-rough at $\alpha = 20°$. The smooth foil generates the lowest drag among the three foil surfaces within the lower α range. Further increase in α leads to C_D increasing on a steeper slope for the smooth foil, prompting a higher drag generation for the smooth foil compared to the rough foils across the Re range.

To better illustrate the differences in C_L and C_D between the foil surfaces, in Fig. 4, we present a direct comparison of the force coefficients for mid-rough (Fig. 4a, b) and full-rough (Fig. 4c, d) against the smooth foil metrics as functions of α and Re. In the heat maps, each tile is colored with the value corresponding to the relative force coefficient obtained at the given α and Re. The blue and red colored tiles indicate reduction and increase in the rough foil metrics, respectively, against the C_L (Fig. 4a, c) or C_D (Fig. 4b, d) obtained for the smooth foil. As can be deduced from the line plots presented in Fig. 2, both mid-rough and full-rough foils have lower C_L compared to the smooth foil. This difference is up to 25% for $\alpha > 6°$ for both rough foils, with the lowest C_L measured for the mid-rough among the three foil surfaces considered. Within the same range, there is a reduction in C_D for both rough foil surfaces indicated by the blue colored tiles. The reduction is higher for the full-rough compared to the mid-rough. At $Re = 17{,}000$, C_D for the rough foils is 3 to 40% lower than the smooth foil for $\alpha \geq 8°$. The roughness coverage on the foils lead to the highest difference at $\alpha = 12°$, as C_L reaches a peak and the stall conditions occur for all three foil surfaces, as shown in Fig. 2. Another emerging trend in our data set is that, across the Re range, the mid-rough experiences higher drag than the full-rough foil.

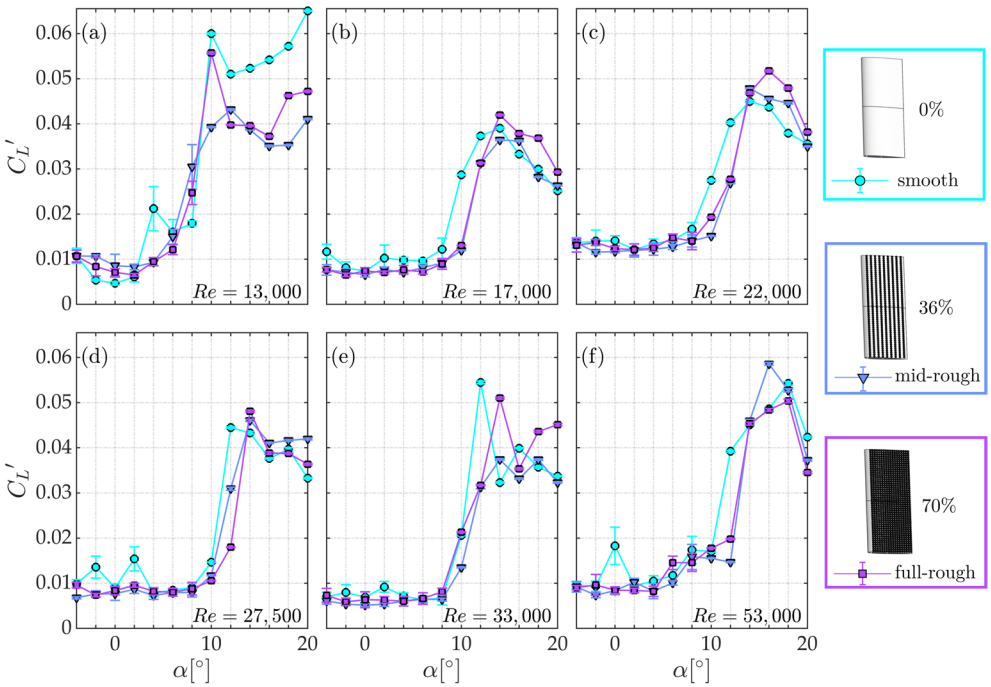

Fig. 5 The normalized root-mean-square of fluctuating lift, C_L', as a function of angle of attack, α, at six different Re within the range of $13{,}000 \leq Re \leq 53{,}000$ in ascending order from a to f. Three foils with different surface roughness coverage ratios; smooth (0%), mid-rough (36%) and full-rough (70%), are plotted with three different symbols, •, ▼, and ■, respectively, as mapped to three different colors shown on the right side of the figure. The errorbars are calculated based on t-distributed error with 95% confidence from 5 repeated tests, as $2.776\sigma_{(.)}/\sqrt{5}$. Here, $\sigma_{(.)}$ is the variation from the reported C_L' or RMS of 5 C_L' values obtained from the repeated tests

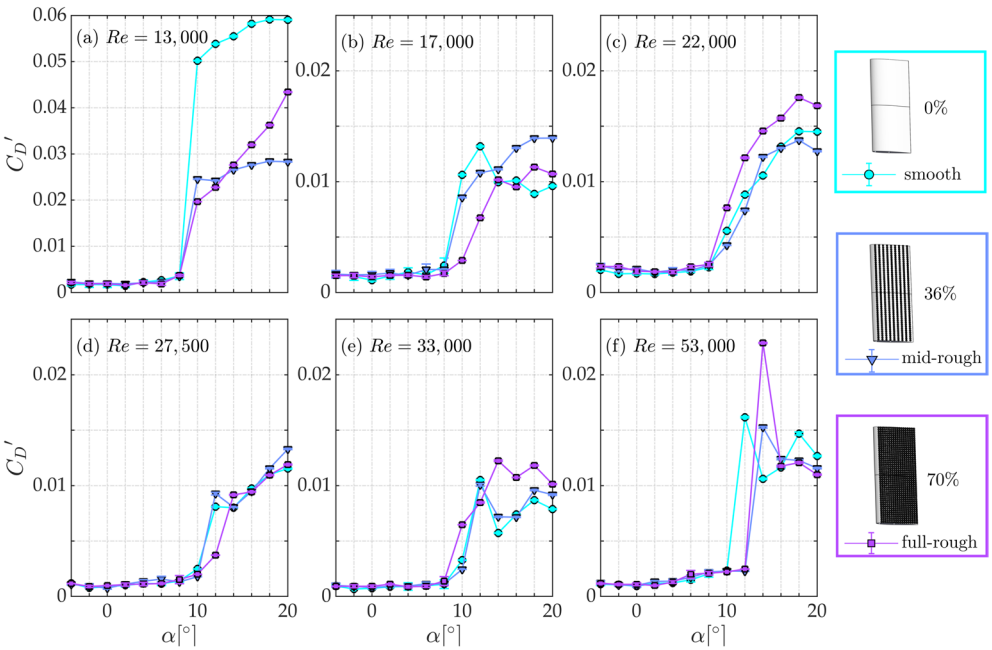

Fig. 6 The normalized root-mean-square of fluctuating drag, C_D', as a function of angle of attack, α, at six different Re within the range of $13{,}000 \leq Re \leq 53{,}000$ in ascending order from a to f. Three foils with different surface roughness coverage ratios; smooth (0%), mid-rough (36%) and full-rough (70%), are indicated with three different symbols, •, ▼, and ■, respectively, as mapped to three different colors and shown on the right side of the figure. The errorbars are calculated based on t-distributed error with 95% confidence from 5 repeated tests, as $2.776\sigma_{(.)}/\sqrt{5}$. Here, $\sigma_{(.)}$ is the variation from the reported C_D' or RMS of 5 C_D' values obtained from the repeated tests

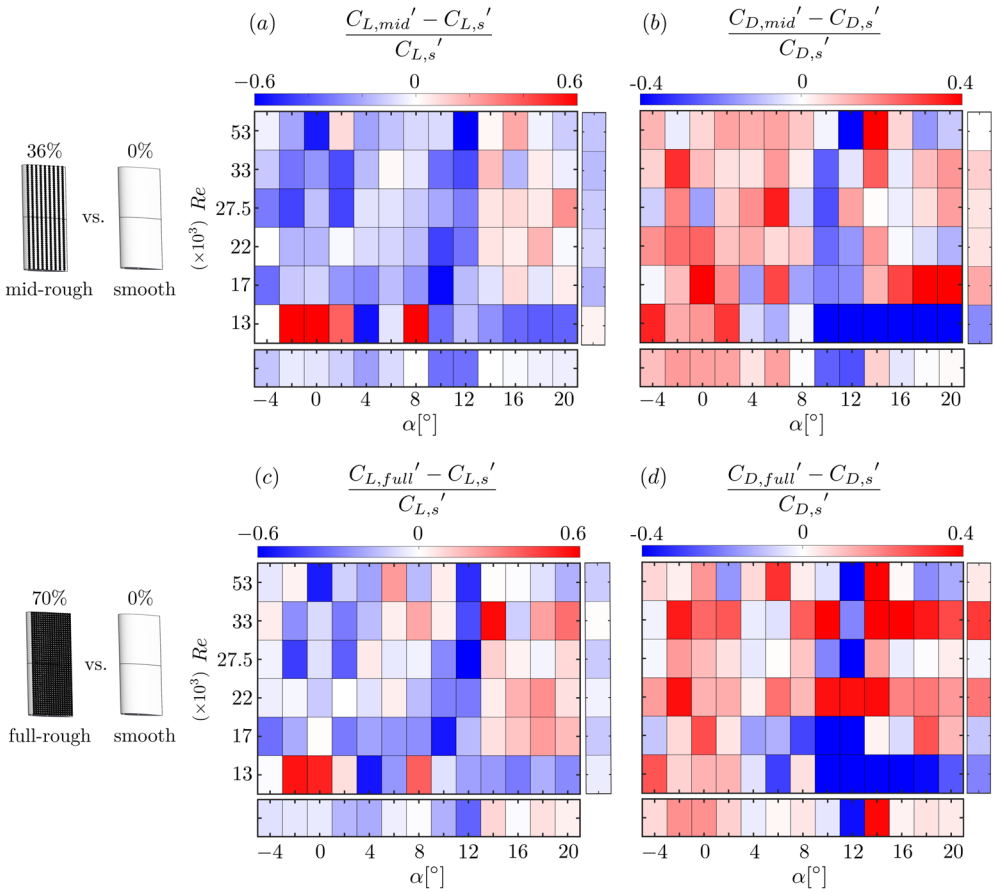

Fig. 7 Lift and drag fluctuations (first and second columns, respectively) of mid-rough (**a**, **b**) and full-rough (**c**, **d**) foils relative to the smooth foil plotted as heat-maps as functions of α and Re. Each tile in the heat maps corresponds to a value for a given α and Re combination. The additional, horizontally and vertically oriented tiles that are located at the bottom and on the right-hand side of the heat maps represent relative fluctuations averaged across all Re for each α and across all α values for each Re, respectively

This difference is more pronounced within the lower angle of attack regime, as shown in Figs. 3 and 4b, d, and can be attributed to the roughness distribution having an influence on the wetted surface area. The flow may perceive full-rough as a thicker smooth foil, whereas, mid-rough distribution, due to larger spacing between the roughness elements along the flow direction, may lead to a more pronounced impact on the foil's drag.

3.2 Instantaneous fluctuations in lift and drag coefficients

The variation in surface roughness can also affect the instantaneous force fluctuations. Figures 5 and 6 show C_L' and C_D' as a function of α at different Re, respectively. Note that C_L' and C_D' are calculated as the averaged non-dimensional RMS values of fluctuating lift and drag obtained from the repeated measurements, respectively. Across the parameter space, the non-dimensional fluctuations in both lift and drag are lower for $\alpha \leq 8°$ with $C_L' \approx 0.01$ and $C_D' \approx 0.002$ and with small variations between the three foil surfaces, except for the lowest Re case where fluctuating force coefficients, C_L' and C_D' have notable differences between the foil surfaces for $\alpha \geq 12°$. Within this region, regardless of Re, C_L' and C_D' dramatically increase with the onset of flow separation, and peak before a downward trend starts as α further increases. This jump in C_L' in Fig. 5 is more pronounced compared to C_D' presented in Fig. 6 around the stall point, except for $Re = 13{,}000$ case, at which both lift and drag fluctuations rise up to comparable values with the reported C_L' and C_D' of ~ 0.06 at $\alpha = 20°$. Regardless of the surface roughness, there is a sudden increase in C_L' and C_D' for $8° \leq \alpha \leq 16°$. There is also a gradual increase in peak C_L' within the same α range as Re increases from 17,000 to 53,000, except for the $Re = 13{,}000$ case where the foil surfaces experience higher amplitudes of lift and drag coefficient fluctuations.

Figure 5b–f shows an increase in lift fluctuations for the smooth foil for $8° \leq \alpha \leq 12°$ and $17{,}000 \leq Re \leq 53{,}000$ compared to rough foils. At $Re = 13{,}000$, there is a sharp increase

in non-dimensional fluctuations of lift and drag across all the foil surfaces within the second half of the α range. Within this range, the mid-rough foil experiences the lowest non-dimensional lift and drag fluctuations, while the fluctuations over the smooth foil rises sharply up to ~ 0.06 levels in both lift and drag directions, as shown in Figs. 5a and 6a. Beyond these observations, the differences in $C_L{}'$ and $C_D{}'$ between the roughness cases are subtle and hard to detect. Thus, to enable a direct comparison, Fig. 7 presents the variation of lift and drag fluctuations of the rough foils relative to the smooth foil as a function of α and Re, as heat maps. The relative fluctuating lift and drag for mid-rough are shown in Fig. 7a and b, and the corresponding data for the full-rough are shown in Fig. 7c and d, respectively. The additional tiles oriented horizontally and vertically, at the bottom and on the right of the heat maps, show relative fluctuation values that are averaged across the Re range at each α, and across the α range at each Re, respectively. Each tile is mapped to the colorbar indicating relative fluctuation levels at the corresponding (α, Re). The negative and positive values of relative fluctuations indicate lower and higher force fluctuations for the mid-rough and full-rough foils compared to the smooth foil, mapped to blue and red colors, respectively. Across all Re, except for $Re = 13{,}000$, roughness on foil surfaces reduces the lift fluctuations for $\alpha \leq 12°$, with the highest reduction obtained when $\alpha \sim 10° - 12°$. Beyond, for $\alpha > 12°$, lift fluctuations increase for both mid-rough and full-rough, up to 25–30% higher than the smooth foil. There is a reversal of this trend at $Re = 13{,}000$. The lift and drag fluctuations are higher for the first half of the α range, and lower for the second half for the rough foils compared to the smooth foil. The overall reduction in $C_L{}'$ for the rough foils compared to the smooth foil in pre-stall conditions cannot be solely explained by lower time-averaged C_L, as the comparison of these two metrics in Fig. 15, $C_L{}'/C_L$ shows lower than 1% difference between the three foil surfaces for $\alpha \leq 8°$, and up to 5% increase for the smooth foil compared to the rough foils for $\alpha \sim 10° - 12°$.

In Fig. 7b and d, the addition of roughness elements on mid-rough and the full-rough foil surfaces leads to higher relative drag fluctuations for most $\alpha - Re$ space. The exception to this trend is for $\alpha \sim 10° - 12°$ range where the onset of stall occurs (Fig. 2), and the rough foil surfaces experience lower $C_L{}'$ and $C_D{}'$, compared to the smooth foil. A comparison of the heat maps presented for the rough foil reveals that the mid-rough foil generally experiences lower

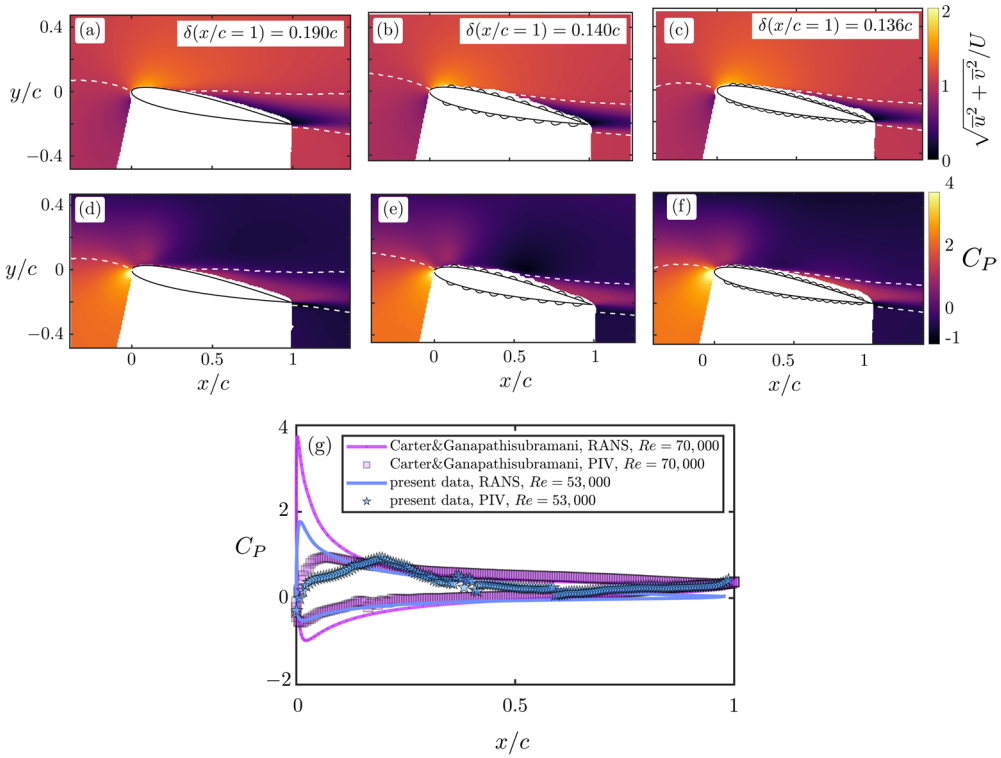

Fig. 8 Comparison of the time-averaged velocity magnitude normalized by the free-stream velocity, $\sqrt{\overline{u}^2 + \overline{v}^2}/U$, and the time-averaged pressure (C_P) plotted for smooth foil in a and d (first column), for mid-rough foil in b and e (second column), and for full-rough in c and f (third column), respectively, at $Re = 53{,}000$ and $\alpha = 12°$. At the bottom, we present a comparison of the reconstructed surface pressure with dynamically matched RANS data, using the smooth foil data in the present work at $Re = 53{,}000$ and a similar data comparison at $Re = 70{,}000$ from (Carter and Ganapathisubramani 2023, 2024)

lift fluctuations and higher drag fluctuations than the full-rough within the considered $\alpha - Re$ space. Both Re averaged (horizontal tiles at the bottom) and α averaged (vertical tiles on the right) values show higher lift fluctuation reduction and an overall increase in drag fluctuations against smooth foil for the mid-rough in Fig. 7a and b compared to full-rough in Fig. 7c and d. The increase in roughness coverage on the foil surfaces from 36% to 70% decreases the reduction in lift fluctuations and leads to an overall increase in drag fluctuations between the mid-rough and full-rough foils.

3.3 Flow-field comparison: time-averaged velocity and pressure

To understand the effect of roughness on the static foil surfaces, we compared the velocity fields and pressure fields reconstructed from planar PIV measurements. We used a Poisson solver approach for the pressure reconstruction as detailed in previous studies (de Kat and Ganapathisubramani 2012; Laskari et al. 2016; Ferreira and Ganapathisubramani 2020; Carter and Ganapathisubramani 2023, 2024). First, we considered the Navier–Stokes momentum equation for two components of the velocity field for incompressible flows:

$$\frac{\partial \mathbf{u}}{\partial t} + \mathbf{u} \cdot \nabla \mathbf{u} = -\frac{1}{\rho}\nabla p + \nu \nabla^2 \mathbf{u} \tag{2}$$

where $\mathbf{u}(\mathbf{x}, t) = (u(\mathbf{x}, t), v(\mathbf{x}, t))$ is the instantaneous velocity vector with streamwise(u) and cross-stream velocity (v) components, $p(\mathbf{x}, t)$ is the planar pressure, ρ is the density and ν is the kinematic viscosity of water. We used Taylor's hypothesis approach to calculate the unsteady velocity term, following the work by de Kat and Ganapathisubramani (2012) and Ferreira and Ganapathisubramani (2020). This method assumes that the fluctuations in the velocity field are convected at a certain velocity $\mathbf{u_c}$ that varies spatially and in time. If the fluctuations are *frozen*, invoking Taylor's hypothesis, the temporal and spatial gradients can be expressed as:

$$\frac{D\mathbf{u}'}{Dt} = \frac{\partial \mathbf{u}'}{\partial t} + (\mathbf{u_c} \cdot \nabla)\mathbf{u}' \tag{3}$$

The substitution into Eq. 2 and taking the divergence of the left and right side of the equation yields:

$$\nabla^2 p_{TH} = \nabla \cdot \{-\rho\{(\mathbf{u}' \cdot \nabla)\mathbf{u} + \left[(\mathbf{u} - \mathbf{u_c}) \cdot \nabla\right]\mathbf{u}' - \nabla^2 \mathbf{u}\}\} \tag{4}$$

where p_{TH} denotes the pressure reconstructed using Taylor's hypothesis in Eq. 4, based on two components of the velocity field. The local convective velocity is assumed to be equal to the time-averaged local velocity, $\mathbf{u_c} = \overline{\mathbf{u}}$, following previous studies (Laskari et al. 2016; Ferreira and Ganapathisubramani 2020; Van der Kindere et al. 2019). To solve Eq. 4, Neumann boundary conditions were applied along the inlet, outlet, and lower boundaries of the domain as well as the foil surface. Using Bernoulli's equation, Dirichlet boundary conditions were applied to the upper boundary. The velocity fluctuations are limited to 2 to 3% of the free-stream velocity in magnitude on the upper boundary. Thus, the flow can be assumed to be irrotational and Bernoulli's equation is expected to hold.

As detailed extensively in previous studies, the convection velocity is scale-dependent and there are limitations for pressure estimations based on snapshot 2D and 3D PIV measurements (Laskari et al. 2016; Ferreira and Ganapathisubramani 2020; Van der Kindere et al. 2019). However, using TH approach based on 2D PIV, it has been shown that the RMS pressure field for flows where shear layer detachment is present can be reconstructed with up to 54% correlation compared to reference pressure measurements (Van der Kindere et al. 2019) and with less than 3% error compared to LES (Large-Eddy Simulation) results (Ferreira

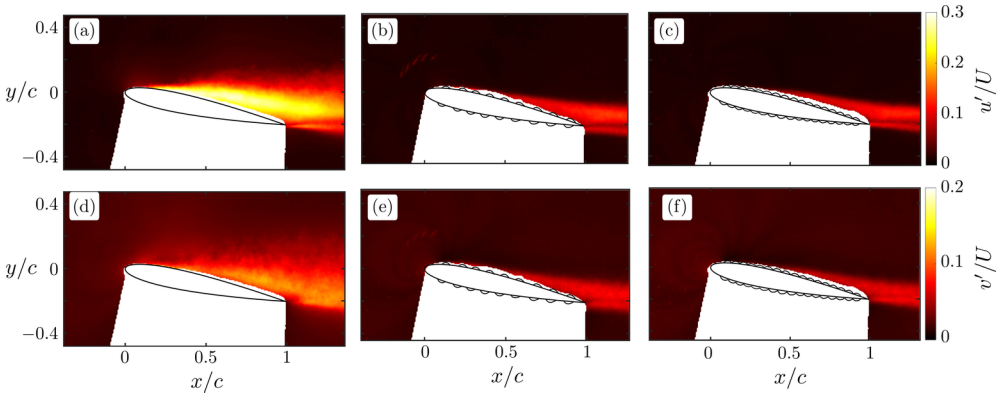

Fig. 9 Comparison of the velocity fluctuations for streamwise (u') and cross-stream (v') components of the velocity field normalized by the free-stream velocity, U, for smooth foil in **a** and **d** (first column), for mid-rough foil in **b** and **e** (second column), and for full-rough in c and f (third column), respectively, at $Re = 53{,}000$ and $\alpha = 12°$

and Ganapathisubramani 2020). Further information on the theoretical background and comparison between different pressure estimation approaches can be found in this reference (Laskari et al. 2016). We would also like to refer to these studies (Van Oudheusden et al. 2007; Carter and Ganapathisubramani 2023, 2024) if further reading is desired on pressure estimation from planar PIV measurements of flows over aero/hydrofoils.

In Fig. 8, the time-averaged velocity magnitude and pressure coefficients are compared between the smooth, mid-rough and full-rough foils at $\alpha = 12°$ and $Re = 53{,}000$. The velocity magnitude over the foil surfaces was normalized by the free-stream velocity in Fig. 8a–c. The time-averaged velocity fields shown in Fig. 8 are qualitatively similar between the roughness cases, despite the subtle differences in the time-averaged boundary layers. The boundary layer has a larger thickness around the trailing edge region for the smooth foil ($\delta_{\text{smooth}} = 0.19c$) compared to mid-rough and full-rough ($\delta_{\text{mid-rough}} = 0.14c$ and $\delta_{\text{mid-rough}} = 0.136c$), as indicated by the white dashed lines, marking $0.99U$ velocity magnitude. This suggests a delay in flow separation and stall for mid-rough and full-rough foils. At $\alpha = 12°$, more advanced flow separation and *intermittently* detached shear layers can lead to a larger velocity deficit around the trailing edge *in time-average* for the smooth foil compared to rough foils. Supporting this, the $C_L(\alpha)$ curves presented in Fig. 2f demonstrate that smooth foil slowly transitions to stall as the angle of attack increases from 10° to 16°. Within the same α range, mid-rough and full-rough foils reach peak lift levels with a delay, at $\alpha = 14°$. These trends in lift correspond to a sudden increase in drag for the smooth foil, as shown in Fig. 3f. At $\alpha = 12°$, drag experienced by the smooth foil is greater in time average, while it is 10–40% lower than the mid-rough and full-rough drag for the lower α range, $-2° \leq \alpha \leq 10°$.

Figure 8d–f presents the time-averaged pressure normalized by the total pressure as, $C_P = \overline{p}/0.5\rho(\overline{u}^2 + \overline{v}^2)$. The reconstructed pressure fields in Fig. 8d–f for the foil surfaces show lower pressure on the suction side (upper foil surface) and higher pressure values around the leading edge due to flow stagnation. The pressure fields show subtle differences between the foil surfaces, as predicted by the small differences in C_L for $\alpha = 12°$ at $Re = 53{,}000$. An additional comparison for the smooth foil pressure reconstruction with a dynamically matched Reynolds averaged Navier Stokes(RANS) simulation at $Re = 53{,}000$ is provided using the reconstructed surface pressure in Fig. 8g, along with a similar pressure reconstruction data comparison previously published for NACA0012 cross-section at Re =70,000 and $\alpha = 13°$ (Carter and Ganapathisubramani 2024). The comparison shows good agreement beyond $x/c \approx 0.2$. The previously reported deviation around the leading edge between the reconstructed pressure and RANS results (Carter and Ganapathisubramani 2024) is found to be smaller for the present data set ($Re = 53{,}000$ and $\alpha = 12°$) for the same foil cross-section. We deemed this comparison as satisfactory, as we will focus mainly on the pressure fluctuations over the foil surfaces for $x/c \geq 0.2$.

4 Discussion

Similar to the time-averaged response of dragon-fly inspired airfoils with leading edge corrugations (Van Bokhorst et al. 2015), our force and flow measurements show subtle alterations in the time-averaged lift and drag forces, corresponding to small changes in the time-averaged velocity fields. The lower C_D at lower Re leads to a slight improvement in the lift-to-drag ratio for full rough relative to the smooth foil,

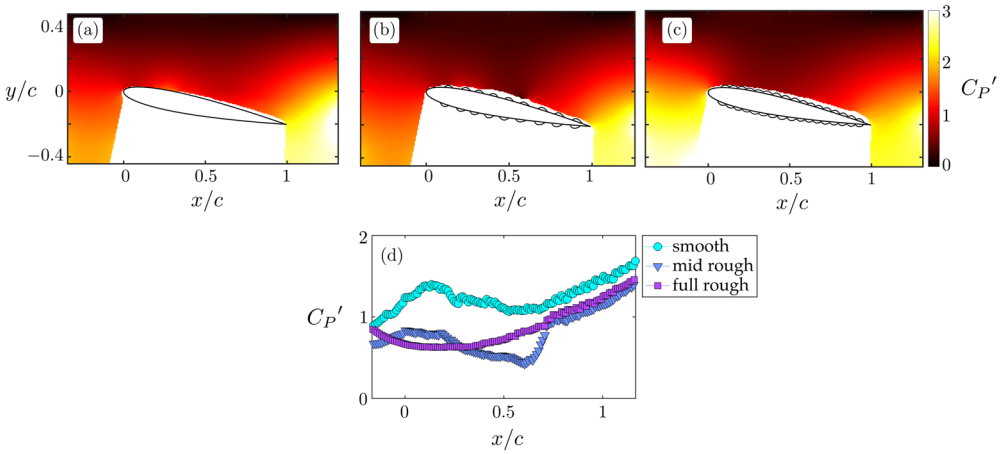

Fig. 10 Comparison of fluctuating pressure fields (C_P') at $Re = 53{,}000$ for smooth (**a**), mid-rough (**b**), and full-rough foils (**c**). Surface pressure fluctuations along the three foil surfaces, as extracted from the region $0.04c$ above the foil surfaces (**d**)

as shown in Fig. 14a and b. This limited range of improvements in C_L/C_D compared to previous findings (Domel et al. 2018a) can be attributed to the difference in roughness geometry, spherical-cap roughness elements used in the present study and shark-skin inspired biomimetic scales. The biomimetic scales tilted in the flow direction covering the suction surface only can create an asymmetry in the foil profile and an upward shift in $C_L - \alpha$ curves with a nonzero lift generation at $\alpha = 0°$ (Domel et al. 2018a).

In contrast, distributed roughness coverage introduce more significant alterations in lift and drag fluctuations, as well as in the corresponding velocity fields.

4.1 Surface roughness leads to delays in stall and reduction in velocity fluctuations

The mid-rough and full-rough foils experience a delay in stall for $Re \geq 27{,}500$. This corresponds to spatially reduced velocity fluctuations and magnitude over rough foil surfaces. Figure 9 compares velocity fluctuations over the foil surfaces at $\alpha = 12°$ and $Re = 53{,}000$ The streamwise velocity fluctuations, u' (first row), and cross-stream velocity fluctuations, v', (second row) are shown over smooth (first column), mid-rough (second column) and full-rough foils (third column) as normalized by U. The flow over the smooth foil fluctuates over a larger area with u' and v' up to $0.3U$ and $0.19U$ over the foil surface, respectively. The increase in the roughness coverage results in a reduction in velocity fluctuations spatially and in magnitude. The mid-rough experiences up to $u' \approx 0.18U$ and $v' \approx 0.12U$, while the fluctuations for full-rough are up to $0.1U$ and $0.11U$ for u' and v', respectively. This suggests that the shear layer detachment and the flow separation are more advanced for the smooth foil compared to mid-rough and full-rough, as predicted by the respective $C_L - \alpha$ and $C_D - \alpha$ curves in Figs. 2f and 3f.

The dynamics of flow separation over finite airfoil or flat plate surfaces is highly complex and driven by changes in Reynolds stresses that occur at low and intermediate reduced frequencies, alternating between re-attachment zones or full-separation (Covert and Lorber 1984; Ambrogi et al. 2023). Surface roughness can act to disrupt these dynamics and reduce flow separation regions passively. A reduction in flow separation region has been reported for surfaces covered with biomimetic, shark-skin-like scales (Du et al. 2022; Afroz et al. 2016; Domel et al. 2018a). However, here, the manipulation of flow separation dynamics is primarily driven by the presence of surface roughness. The ridges and tilt angle aligned in the flow direction can act to enhance this mechanism further (Du et al. 2022), noting that their performance likely depends on the preferential flow direction. In such applications, the profile drag primarily depends on the shape and cross-section of the foil. Non-preferential flow directions can lead to further increase in profile drag, if the surface features are tilted in one direction. Assuming appropriate choice of foil shape, the roughness elements with surface symmetry, such as spherical-cap elements, can prove to be more versatile in flow scenarios where the flow direction varies relative to the foil surface.

4.2 Surface roughness leads to reductions in lift fluctuations

The surface roughness on the foil surfaces alters the transient response of lift generation and leads to an overall decrease in lift fluctuations relative to the smooth foil for $-2° \leq \alpha \leq 12°$ as shown in Fig. 7. The reduction in lift fluctuations decreases as the roughness coverage increases from 35% to 70% between the mid-rough and the full-rough foils. The decrease in lift fluctuations can be linked to the fluctuations in pressure over the rough foil surfaces.

In Fig. 10a–c, the pressure fluctuations over the foil surfaces were presented for smooth, mid-rough and full-rough, respectively, at $Re = 53{,}000$. ${C_P}'$ vary spatially along the foil surfaces depending on the surface roughness. There are larger variations in pressure along the smooth surface with ${C_P}' > 1$ for the entire foil surface, whereas mid-rough and full-rough maintain lower magnitudes of pressure fluctuations with ${C_P}' < 1$ for the range of $0.1 \leq x/c \leq 0.7$ across the foil surfaces. This difference in ${C_P}'$ between the foil surfaces is more clear once the surface pressure fluctuations are compared. ${C_P}'$ is extracted from the area $0.04c$ above the foil surfaces, and plotted as a function of chord location in Fig. 10d. For all three surfaces, ${C_P}'$ near foil surfaces gradually increase as the boundary layer development and flow separation occur toward the trailing edge. The presence of roughness on the foil surfaces lowers the pressure fluctuations for mid-rough and full-rough, where mid-rough experiences slightly lower fluctuations compared to both smooth and full-rough. The corresponding reduction of ${C_L}'$ shown in Figs. 5 and 7 for mid-rough and full-rough are directly linked to the lower fluctuations in surface pressure presented in Fig. 10d. At $\alpha = 12°$ and $Re = 53{,}000$, the reductions in lift fluctuations for mid-rough and full-rough foils are up to $\sim 62\%$ and $\sim 49\%$ relative to the smooth foil control surface.

4.3 Surface roughness and drag reduction considerations

In our data set, the spherical-cap elements reduce the drag on foil surfaces only for low-Re conditions, at $Re = 13{,}000$ and 17,000 for pre-stall conditions. We found up to 4.3% drag reduction at $Re = 13{,}000$ for full-rough, and up to 12% and 21% drag reduction for both mid-rough and full-rough, respectively, at $Re = 17{,}000$ for $\alpha < 10°$. At higher α, especially for the stall conditions, this reduction increases up to

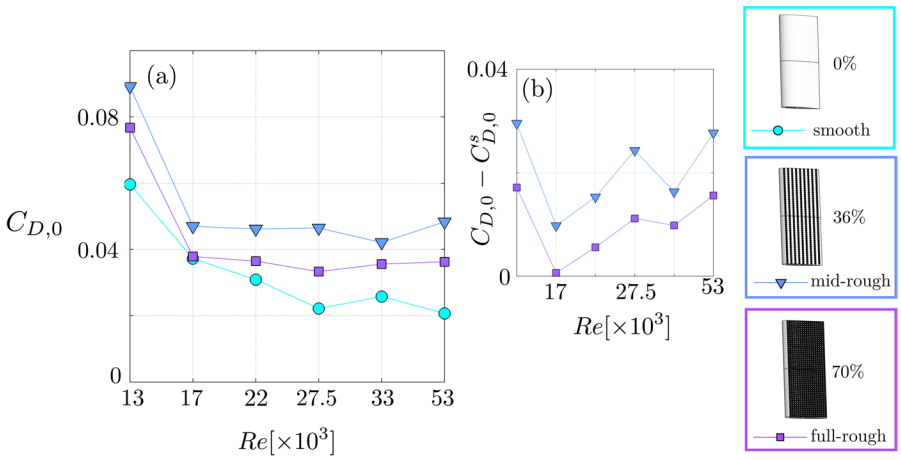

Fig. 11 The drag coefficient measured at $\alpha = 0°$, denoted as $C_{D,0}$, against Re for all foil surfaces (**a**). The change in $C_{D,0}$ with the addition of roughness coverage for the two rough foil surfaces compared to the smooth foil surface, denoted as $C_{D,0} - C^s_{D,0}$, against Re (**b**). Three foils with different surface roughness ratios; smooth (0%), mid-rough (36%) and full-rough (70%), are plotted with three different symbols, •, ▼, and ■, respectively, as mapped to three different colors shown on the right side of the figure

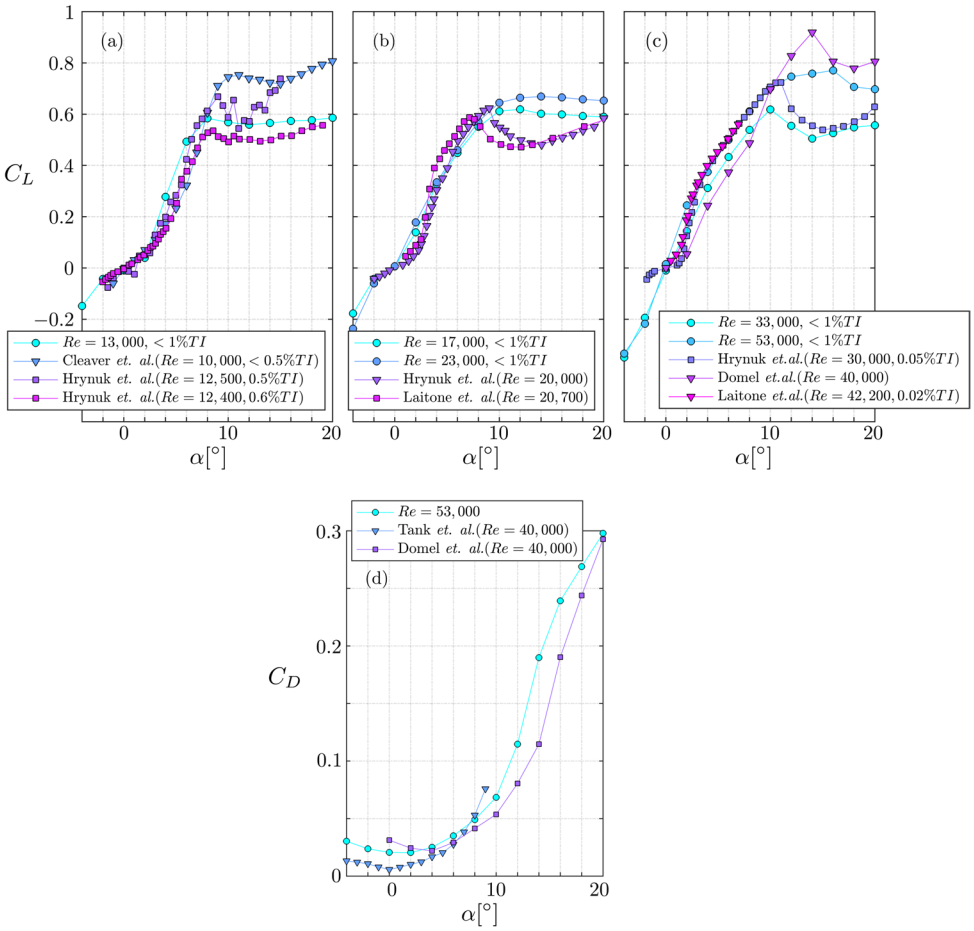

Fig. 12 A comparison of C_L from present data set at $Re = 13{,}000$ (**a**), $Re = 17{,}000$ and $Re = 23{,}000$ (**b**), and $Re = 33{,}000$ and $Re = 53{,}000$ (**c**) and a comparison of C_D at $Re = 53{,}000$ is provided against a set of digitized data from relevant previous work for similar dynamic conditions (Laitone 1997; Cleaver et al. 2010; Tank et al. 2017; Domel et al. 2018a; Hrynuk et al. 2024). In the legend, where possible, we have indicated the turbulence intensity within the test facilities, as the stall behavior and measured C_L for pre-stall and post-stall conditions can be significantly affected by the inflow turbulence metrics

40%. For higher Re, foils with roughness have higher time-averaged drag than the smooth foil in pre-stall conditions, as shown in Fig. 3. This is consistent with previous findings from flat plates with micro biomimetic scales experiencing drag reduction within low to moderate Re range, and higher drag for Re greater than 50,000 (Domel et al. 2018b). The reduction measured for the foil surfaces is very well within the computational predictions based on riblets in laminar boundary layer flows (Raayai-Ardakani and McKinley 2019). The use of smaller size denticles and further manipulation of the ratio between the spacing and roughness protrusion height may provide a larger Re range of drag reduction

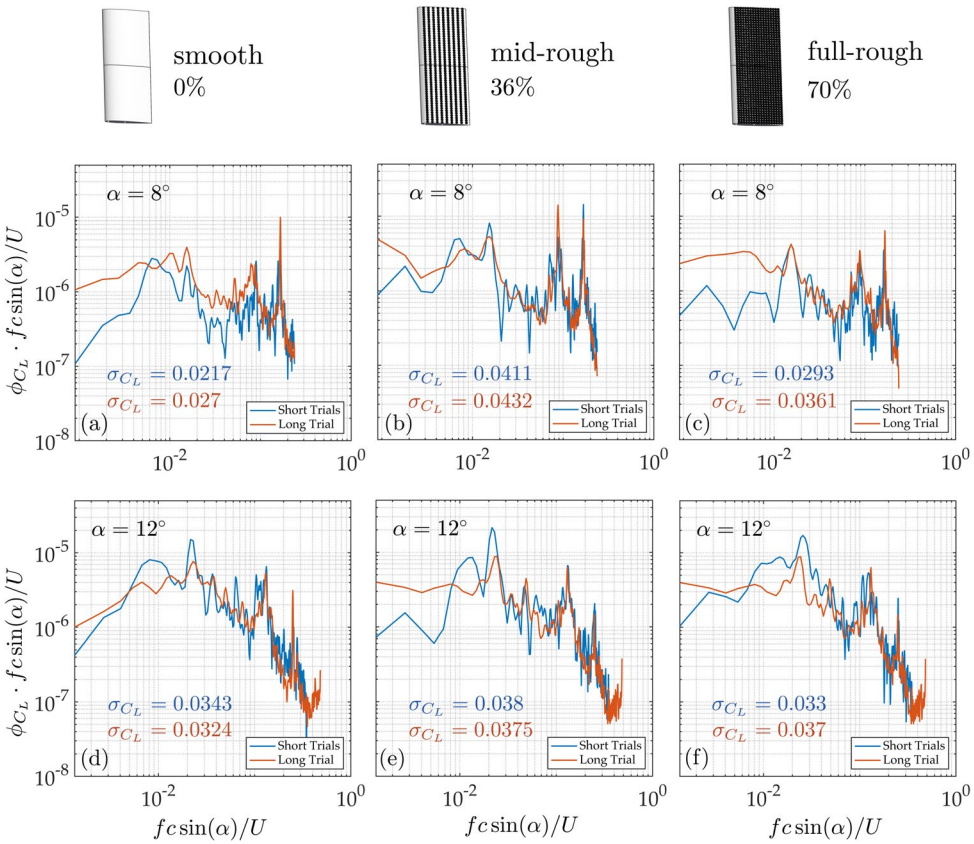

Fig. 13 Comparison of power spectral density calculated from lift forces (ϕ_{C_L}) and pre-multiplied by reduced frequency ($fc\sin(\alpha)/U$) plotted against reduced frequency computed from the shorter runs (average ϕ_{C_L} from 5 repeated tests of $\sim$ 100 convection cycles) and the longer runs ($\sim$ 500 convection cycles) for the smooth and the rough foils. Here, the rows present foil data at $\alpha = 8°$ and 12°, and each column corresponds to the smooth (**a**, **d**), the mid-rough (**b**, **e**) and the full-rough (**c**, **f**) foils. The RMS values calculated from each PSD curve is inserted as σ_{C_L} to the plots, as mapped to blue (shorter trials) and orange (long trial) colors

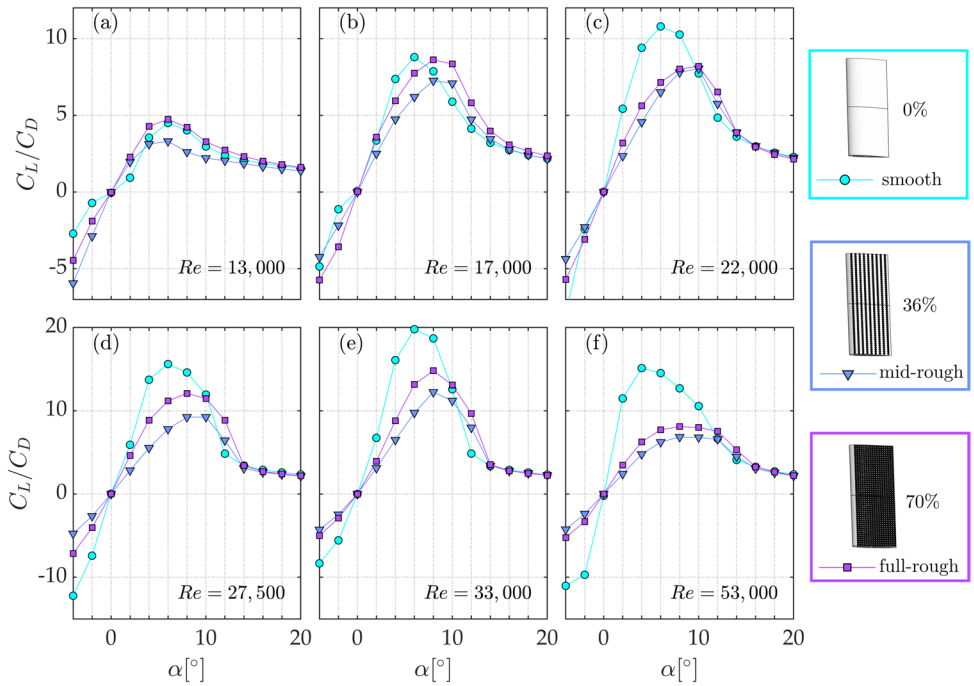

Fig. 14 Lift to drag ratio, C_L/C_D, as a function of angle of attack, α, for the Re range of $13{,}000 \leq Re \leq 53{,}000$ in ascending order from a to f. Three foils with different surface roughness ratios; smooth (0%), mid-rough (36%) and full-rough (70%), are plotted with three different symbols, •, ▼, and ■, respectively, as mapped to three different colors shown on the right side of the figure

for rough foil surfaces (Domel et al. 2018b; Raayai-Ardakani and McKinley 2019).

Determination of the roughness function directly for the rough foil surfaces is out of the scope of this work. However, considering the total drag experienced by the smooth and rough foil surfaces at $\alpha = 0°$, we can comment on which surface may deliver the largest roughness function. If the frictional Reynolds number matches between the rough and

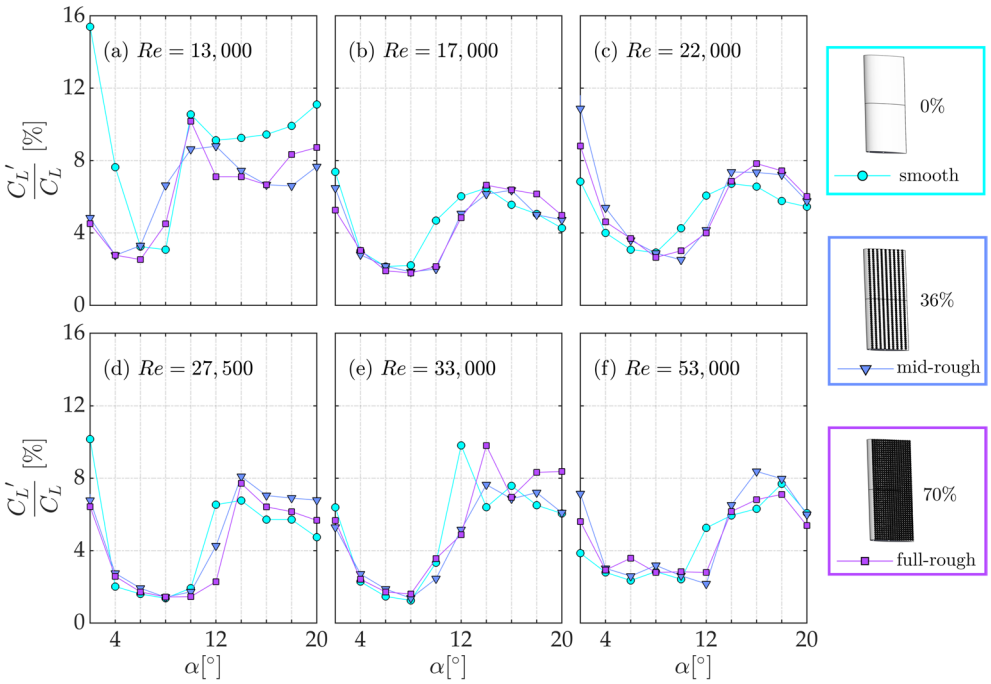

Fig. 15 The ratio of fluctuations over time-averaged lift coefficient, C_L'/C_L, as a function of angle of attack, α, for the Re range of $13{,}000 \leq Re \leq 53{,}000$ in ascending order from a to f. Three foils with different surface roughness ratios; smooth (0%), mid-rough (36%) and full-rough (70%), are plotted with three different symbols, •, ▼, and ■, respectively, as mapped to three different colors shown on the right side of the figure

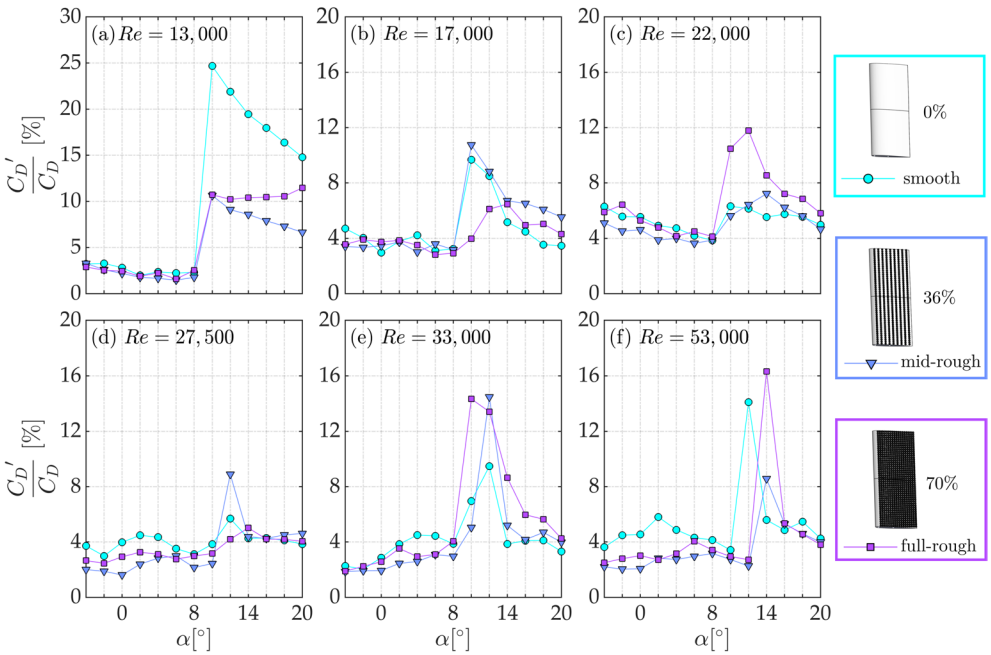

Fig. 16 The ratio of fluctuations over time-averaged drag coefficient, C_D'/C_D, as a function of angle of attack, α, for the Re range of $13{,}000 \leq Re \leq 53{,}000$ in ascending order from a to f. Three foils with different surface roughness ratios; smooth (0%), mid-rough (36%) and full-rough (70%), are plotted with three different symbols, •, ▼, and ■, respectively, as mapped to three different colors shown on the right side of the figure

smooth surfaces in the presence of outer layer similarity, then, the differences in skin friction coefficient can provide a measure for roughness function (Medjnoun et al. 2023). The change in total skin friction (viscous drag) of the foil surfaces due to roughness at $\alpha = 0°$ can then be expressed as proportional to the roughness function, $C_F(\alpha = 0°) \propto f(\Delta U^+)$. At $\alpha = 0°$, since the foil surfaces experience zero induced drag due to $C_L = 0$, the total drag ($C_{D,0}$) becomes a combination of profile drag or pressure drag ($C_{D,p}$) and the viscous drag (C_F), $C_{D,0} = C_{D,p} + C_F$. Here, there is often a trade-off between skin friction and the profile drag in determination of the effect of roughness on finite surfaces (Beratlis et al. 2019). For simplification, we will neglect the alterations in $C_{D,p}$ due to roughness and assume equivalent profile drag at $\alpha = 0°$ between the foil surfaces. Then, we can have a measure of roughness function, with a closer inspection of the change in $C_{D,0}$ by isolating the roughness contribution to C_F. Figure 11a presents $C_{D,0}$ against the *Re* range considered for the smooth and rough foil surfaces, where the drag coefficient decreases as the *Re* increases, as expected. The mid-rough foil experiences the highest $C_{D,0}$ across the *Re* range. We can isolate the roughness related contributions by subtracting the smooth foil drag coefficient ($C^s_{D,0}$) from rough foil cases. We present this difference, $C_{D,0} - C^s_{D,0}$, against *Re* in Fig. 11b. Based on this comparison, we can speculate that the mid-rough surface would deliver the largest roughness function.

The time-averaged drag results for rough foils show that the full-rough maintains lower drag than the mid-rough foil across the parameter space. This difference is the largest at $Re = 13{,}000$. Although the spatial resolution of the flow measurements does not allow us to further investigate this trend, the existing literature on wall-bounded flows over rough boundaries provides further insights as to what might have caused this trend. In the present data set, while the roughness protrusion is the same, the roughness spacing between the peaks of roughness elements is two times larger for the mid-rough ($\sim$ 10H) relative to full-rough ($\sim$ 5 H). This difference in roughness spacing can lead to *wake sheltering* of roughness elements, reducing drag(Jiménez 2004; Chung et al. 2021). When the roughness spacing is larger than 3–4H, the interactions between roughness elements become weaker, and each element can generate its own independent wake. When spacing is less than 3–4H, the closer flow interactions can result in vortex formation, embedded between the roughness elements, creating a buffer that cushions the flow and decreases the wetted surface area. This type of flow mechanism is previously observed for shark denticles with spatial distance reduced due to bristling effects (Lang et al. 2008). In the present data set, the alternating flow scenarios between the two regimes can act to decrease the wetted surface area for full-rough foil. This offers a possible explanation for the higher time-averaged drag measured for mid-rough relative to full-rough, as shown in Fig. 3 and detailed in Sect. 3.1. To confirm this hypothesis, a more systematic investigation is required, resolving the flow interactions between the roughness elements across different roughness arrangements.

5 Conclusions

We measured force and flow over rough foils covered with spherical-cap roughness elements. The foil surfaces with three different roughness coverage ratios have been used, smooth (0%), mid-rough (36%), and full-rough (70%), surveying a moderate *Re* range of $10{,}000 \leq Re \leq 55{,}000$ and an angle of attack range of $-2° \leq \alpha \leq 20°$. The measured lift and drag forces show that spherical-cap roughness elements have a larger influence on the instantaneous response of the rough foils compared to the time-averaged forces. The rough foils experience a small decrease in time-averaged lift and an increase in time-averaged drag for $\alpha < 10°$ compared to the smooth foil except for lower *Re* cases where time-averaged drag is 4 to 21% lower for the rough foils relative to the smooth foil. In contrast, surface roughness has a more significant impact on the fluctuating forces and the flow over the foil surfaces. The flow measurements show that surface roughness lowers the velocity fluctuations over the foil surfaces, leading to a delay in flow separation at higher angles of attack, evidenced by the $C_L - \alpha$ curves. The rough foils exhibit reductions in lift fluctuations up to $\sim$ 60% and an increase in drag fluctuations up to $\sim$ 30% compared to the smooth foil for $\alpha < 10°$. Overall, the fluctuations in lift and drag decrease as the roughness coverage varies from full-rough to mid-rough, which corresponds to lower pressure fluctuations over the rough foil surfaces, as shown by the reconstructed pressure fields using planar PIV measurements. Our findings underline the influence of roughness distribution on the instantaneous force response and the flow over the static foil surfaces and reveal passive boundary layer and flow separation control mechanisms enabled by simple surface design considerations.

Appendix A: Comparison of the smooth foil with relevant literature

We present a comparison of our data in Fig. 12 with the digitized experimental data from relevant literature for moderate Reynolds number conditions (Laitone 1997; Cleaver et al. 2010; Tank et al. 2017; Domel et al. 2018b; Hrynuk et al. 2024). As emphasized in previously published work, it is hard to have a good agreement for measurements taken in different facilities and using different numerical approaches, for this moderate Reynolds number range, $Re < 10^6$, even for

a canonical cross-section like NACA0012 (Tank et al. 2017). The flow measures like inflow turbulence intensity and flow events like formation of laminar separation bubbles, flow detachment/reattachment can significantly affect the lift and drag coefficient values experimentally or numerically obtained for static foil cross-sections, especially for stall/post-stall conditions. Nonetheless, we provide a comparison for C_L and C_D values for our data and several other relevant work from the existing literature. Although, we have reasonable agreement for the pre-stall conditions between the data sets, as expected, deviations between data sets do occur for the stall and post-stall conditions. In this work, our focus is mainly on the comparison of the foil surfaces with different roughness coverage. We used the same foil by changing its roughness coverage. We conducted our measurements in the same flow facility. Thus, we find this comparison with the relevant literature to be satisfactory.

Appendix B: Power spectra of lift forces and comparison of fluctuating and time-averaged force coefficients

A comparison of the Power Spectral Density(PSD) curves at $Re = 13{,}000$ for two different angles of attack is provided in Fig. 13. The RMS value of a signal can be computed as the square root of the area under its PSD curve. The shorter test duration of 100 convection cycles is chosen based on the PSD agreement of lift coefficient fluctuations between the long trials and the average of short trials, so that the difference in computed root-mean-square(RMS) of the measurements is within 20% of the RMS value obtained from the longer test. The disagreement of PSD at low frequencies leads to a difference in RMS values up to 20% at $Re = 13{,}000$, which is the highest recorded difference in our data set.

In Fig. 14, we present the lift-to-drag ratio obtained for all three foil surfaces at each α and Re. Similar to the comparison line plots presented in §3.1 and §3.2, the values obtained for each foil surface are mapped to different colors indicated by the schematic on the right and the results are arranged to present our findings at each Re in ascending order. Overall, C_L/C_D increases for all three foil surfaces as the Re increases from 13,000 to 33,000. At $Re = 53{,}000$, the values indicate lower lift against drag for both the smooth and the rough foils, compared to $Re = 33{,}000$. All three foil surfaces exhibit similar lift-to-drag ratio with small differences at $Re = 13{,}000$. As Re increases, the smooth foil C_L/C_D increases compared to the rough foils. Across the Re considered, the mid-rough foil experiences the lowest C_L/C_D amongst the three foils surfaces.

In Figs. 15 and 16, we present the ratios of $C_L{}'$ and $C_D{}'$ to the corresponding time-averaged C_L and C_D, for all three foil surfaces. In Fig. 15, lift fluctuations vary within the range of $2\% \leq C_L{}'/C_L \leq 12\%$ across the parameter space, whereas drag fluctuation ratios increase up to 25% for the smooth foil within the same range in Fig. 16. The fluctuation ratios, both $C_L{}'/C_L$ and $C_D{}'/C_D$, are the highest at $Re = 13{,}000$ for $\alpha \geq 10°$ in both Figs. 15a and 16a. Overall, all three foil surfaces experience an increase in fluctuations relative to the time-averaged coefficient beyond $\alpha = 8°$, which is another indicator of the onset of flow separation within this α range, as discussed in §3.1. The foil surfaces follow similar trends with higher $C_L{}'/C_L$ for the smooth foil compared to the rough foils within $6° \leq \alpha \leq 14°$, which leads to delays in stall. The smooth foil has higher $C_D{}'/C_D$ for the first half of the α range across the Re range, except for $Re = 13{,}000$, where the smooth foil fluctuations are higher than the rough foils across the entire α range.

Acknowledgements We gratefully acknowledge funding from EPSRC (Grant no: EP/W026090/1). MK would like to acknowledge Uttam Cadambi Padmanaban for his assistance in obtaining the RANS results used for surface pressure comparison. She also gratefully acknowledges Dr. Douglas Carter for his insightful discussions on the pressure reconstruction aspects of this work.

Author contributions MK: Investigation, Formal analysis, Methodology, Writing—Original Draft, Writing—Review and Editing, RVG: Methodology, Investigation, Writing—Review and Editing GW: Writing—Review and Editing, Supervision, BG: Conceptualization, Supervision, Funding acquisition, Writing—Review and Editing.

Data availability All data presented in the figures will be made available via University of Southampton's repository upon publication.

Declarations

Conflict of interest The authors declare no conflict of interest.

References

Achenbach E (1971) Influence of surface roughness on the cross-flow around a circular cylinder. J Fluid Mech 46(2):321–335

Afroz F, Lang A, Habegger ML, Motta P, Hueter R (2016) Experimental study of laminar and turbulent boundary layer separation control of shark skin. Bioinspir Biomimet 12(1):016009
Ambrogi F, Piomelli U, Rival DE (2023) Characterisation of unsteady separation in a turbulent boundary layer: reynolds stresses and flow dynamics. J Fluid Mech 972:36
Bearman PW, Harvey JK (1976) Golf ball aerodynamics. Aeronaut Q 27(2):112–122
Bechert D, Bruse M, Hage W, Meyer R (2000) Fluid mechanics of biological surfaces and their technological application. Naturwissenschaften 87(4):157–171
Beratlis N, Balaras E, Squires K (2019) On the origin of the drag force on dimpled spheres. J Fluid Mech 879:147–167
Carter DW, Ganapathisubramani B (2023) Data-driven determination of low-frequency dipole noise mechanisms in stalled airfoils. Exp Fluids 64(2):41
Carter D, Ganapathisubramani B (2024) Low-order planar pressure reconstruction of stalled airfoils using particle image velocimetry data. Phys Rev Fluids 9(1):014602
Choi H, Moin P, Kim J (1993) Direct numerical simulation of turbulent flow over riblets. J Fluid Mech 255:503–539
Chowdhury H, Loganathan B, Wang Y, Mustary I, Alam F (2016) A study of dimple characteristics on golf ball drag. Proc Eng 147:87–91
Chung D, Hutchins N, Schultz MP, Flack KA (2021) Predicting the drag of rough surfaces. Ann Rev Fluid Mech 53:439–471. https://doi.org/10.1146/annurev-fluid-062520-115127
Cleaver D, Wang Z, Gursul I (2010) Vortex mode bifurcation and lift force of a plunging airfoil at low reynolds numbers. In: 48th AIAA Aerospace Sciences Meeting Including the New Horizons Forum and Aerospace Exposition, p 390
Colebrook CF, White CM (1937) Experiments with fluid friction in roughened pipes. Proc R Soc Lond Ser A Math Phys Sci 161(906):367–381
Covert EE, Lorber PF (1984) Unsteady turbulent boundary layers in adverse pressure gradients. AIAA J 22(1):22–28
Dean B, Bhushan B (2010) Shark-skin surfaces for fluid-drag reduction in turbulent flow: a review. Philos Trans R Soc A Math Phys Eng Sci 368(1929):4775–4806
Domel AG, Domel G, Weaver JC, Saadat M, Bertoldi K, Lauder GV (2018) Hydrodynamic properties of biomimetic shark skin: effect of denticle size and swimming speed. Bioinspir Biomim 13(5):056014
Domel AG, Saadat M, Weaver JC, Haj-Hariri H, Bertoldi K, Lauder GV (2018) Shark skin-inspired designs that improve aerodynamic performance. J R Soc Interface 15(139):20170828
Du Z, Li H, Cao Y, Wan X, Xiang Y, Lv P, Duan H (2022) Control of flow separation using biomimetic shark scales with fixed tilt angles. Exp Fluids 63(10):158
Ehrmann RS, Wilcox B, White EB, Maniaci DC (2017) Effect of surface roughness on wind turbine performance. Technical report, Sandia National Lab.(SNL-NM), Albuquerque, NM (United States)
Ferreira MA, Ganapathisubramani B (2020) Piv-based pressure estimation in the canopy of urban-like roughness. Exp Fluids 61(3):70
Gad-el-Hak M, Bushnell DM (1991) Separation control. J Fluids Eng 113:5–30
García-Mayoral R, Jiménez J (2011) Drag reduction by riblets. Philos Trans R Soci A Math Phys Eng Sci 369(1940):1412–1427
Guo P, Zhang K, Yasuda Y, Yang W, Galipon J, Rival DE (2021) On the influence of biomimetic shark skin in dynamic flow separation. Bioinspir Biomim 16(3):034001
Hrynuk JT, Bohl DG (2020) The effects of leading-edge tubercles on dynamic stall. J Fluid Mech 893:5
Hrynuk JT, Olson D, Stutz C, Jackson J (2024) Effects of turbulence on naca 0012 airfoil performance at low reynolds number. AIAA J 62(1):409–417
Hutchins N, Ganapathisubramani B, Schultz M, Pullin D (2023) Defining an equivalent homogeneous roughness length for turbulent boundary layers developing over patchy or heterogeneous surfaces. Ocean Eng 271:113454
Jiménez J (2004) Turbulent flows over rough walls. Ann Rev Fluid Mech 36:173–196
Kat R, Ganapathisubramani B (2012) Pressure from particle image velocimetry for convective flows: a taylor's hypothesis approach. Meas Sci Technol 24(2):024002
Kindere J, Laskari A, Ganapathisubramani B, De Kat R (2019) Pressure from 2d snapshot piv. Exp Fluids 60:1–18
Knight M, Wenzinger CJ (1929) Wind-tunnel tests on a series of wing models through a large angle of attack range. part I: force tests. Annual Report–National Advisory Committee for Aeronautics
Kuethe AM (1972) Effect of streamwise vortices on wake properties associated with sound generation. J Aircr 9(10):715–719
Laitone E (1997) Wind tunnel tests of wings at reynolds numbers below 70 000. Exp Fluids 23(5):405–409
Lang A, Motta P, Hidalgo P, Westcott M (2008) Bristled shark skin: a microgeometry for boundary layer control? Bioinspir Biomim 3(4):046005
Laskari A, Kat R, Ganapathisubramani B (2016) Full-field pressure from snapshot and time-resolved volumetric PIV. Exp Fluids 57:1–14
Lin JC (2002) Review of research on low-profile vortex generators to control boundary-layer separation. Prog Aerosp Sci 38(4–5):389–420
Lissaman P (1983) Low-reynolds-number airfoils. Annu Rev Fluid Mech 15(1):223–239
Massey J, Ganapathisubramani B, Weymouth GD (2023) A systematic investigation into the effect of roughness on self-propelled swimming plates. J Fluid Mech 971:39
McMasters JH, Henderson ML (1979) Low-speed single-element airfoil synthesis. NASA. Langley Res. Center The Sci. and Technol. of Low Speed and Motorless Flight, Pt. 1
Medjnoun T, Aguiar Ferreira M, Reinartz R, Nugroho B, Monty J, Hutchins N, Ganapathisubramani B (2023) Assessment of aerodynamic roughness parameters of turbulent boundary layers over barnacle-covered surfaces. Exp Fluids 64(11):169
Menon K, Mittal R (2020) Aerodynamic characteristics of canonical airfoils at low Reynolds numbers. AIAA J 58(2):977–980
Miklosovic D, Murray M, Howle L, Fish F (2004) Leading-edge tubercles delay stall on humpback whale (megaptera novaeangliae) flippers. Phys Fluids 16(5):39–42
Monty J, Dogan E, Hanson R, Scardino A, Ganapathisubramani B, Hutchins N (2016) An assessment of the ship drag penalty arising from light calcareous tubeworm fouling. Biofouling 32(4):451–464
Moody LF (1944) Friction factors for pipe flow. Trans Am Soc Mech Eng 66(8):671–678
Moria H, Chowdhury H, Alam F, Subic A (2010) Comparative aerodynamic analysis of commercial swimsuits. Sports Technol 3(4):261–267
Muthuramalingam M, Puckert DK, Rist U, Bruecker C (2020) Transition delay using biomimetic fish scale arrays. Sci Rep 10(1):14534
Raayai-Ardakani S, McKinley GH (2019) Geometric optimization of riblet-textured surfaces for drag reduction in laminar boundary layer flows. Phys Fluids 31:5
Santos LM, Lang A, Wahidi R, Bonacci A, Gautam S, Devey S, Parsons J (2021) Passive separation control of shortfin Mako

shark skin in a turbulent boundary layer. Exp Thermal Fluid Sci 128:110433

Tank J, Smith L, Spedding G (2017) On the possibility (or lack thereof) of agreement between experiment and computation of flows over wings at moderate reynolds number. Interf Focus 7(1):20160076

Taylor H, et al (1947) The elimination of diffuser separation by vortex generators. united aircraft corporation report. Technical report, R-4012-3 (R4012-3), Moscow, Russia

Van Bokhorst E, De Kat R, Elsinga GE, Lentink D (2015) Feather roughness reduces flow separation during low reynolds number glides of swifts. J Exp Biol 218(20):3179–3191

Van Oudheusden BW, Scarano F, Roosenboom EW, Casimiri EW, Souverein LJ (2007) Evaluation of integral forces and pressure fields from planar velocimetry data for incompressible and compressible flows. Exp Fluids 43:153–162

Vilumbrales-Garcia R, Kurt M, Weymouth GD, Ganapathisubramani B (2024) Effects of surface roughness on the propulsive performance of pitching foils. J Fluid Mech 982:1

Vinnes MK, Hearst RJ (2021) Aerodynamics of an airfoil with leading-edge icing. Wind Energy 24(8):795–811

Walker JM, Flack KA, Lust EE, Schultz MP, Luznik L (2014) Experimental and numerical studies of blade roughness and fouling on marine current turbine performance. Renew Energy 66:257–267

Ward M, Passmore M, Spencer A, Hanson H, Lucas T (2023) The effect of surface geometry on the aerodynamic behaviour of a football. Sports Eng 26(1):33

Yasuda Y, Zhang K, Sasaki O, Tomita M, Rival D, Galipon J (2019) Manufacturing of biomimetic silicone rubber films for experimental fluid mechanics: 3d printed shark skin molds. J Electrochem Soc 166(9):3302